Article

Corneal Surface Wave Propagation Associated with Intraocular Pressures: OCT Elastography Assessment in a Model Eye

Guoqin Ma [1], Jing Cai [2], Rijian Zhong [2], Weichao He [2], Haoxi Ye [2], Chaitanya SS Duvvuri [3], Chengjin Song [2], Jinping Feng [4], Lin An [5], Jia Qin [5], Yanping Huang [2,5], Jingjiang Xu [2,5], Michael D Twa [3], and Gongpu Lan [2,5,*]

[1] School of Mechatronic Engineering and Automation, Foshan University, Foshan, Guangdong, China.
[2] Guangdong-Hong Kong-Macao Intelligent Micro-Nano Optoelectronic Technology Joint Laboratory, School of Physics and Optoelectronic Engineering, Foshan University, Foshan, Guangdong, China.
[3] College of Optometry, University of Houston, Houston, TX, United States.
[4] Institute of Engineering and Technology, Hubei University of Science and Technology, Xianning, Hubei, China.
[5] Innovation and Entrepreneurship Teams of Guangdong Pearl River Talents Program, Weiren Meditech Co., Ltd., Foshan, Guangdong, China.
* Correspondence: langongpu@fosu.edu.cn.

Abstract: Assessing corneal biomechanics *in vivo* has long been a challenge in the field of ophthalmology. Although recent wave-based optical coherence elastography (OCE) methods have shown promise in this area, the effect of intraocular pressure (IOP) on mechanical wave propagation in the cornea remains unclear. To address this, we constructed an artificial eye model and performed surface wave OCE measurements in the radial directions (54–324°) of the silicone cornea at varying IOP levels (10–40 mmHg). The results demonstrated increases in wave propagation speeds (mean ± STD) from 6.55 ± 0.09 m/s (10 mmHg) to 9.82 ± 0.19 m/s (40 mmHg), leading to an estimate of Young's modulus, which increased exponentially from 145.23 ± 4.43 kPa to 326.44 ± 13.30 kPa. Our implementation of an artificial eye model highlighted that the impact of IOP on Young's modulus (ΔE = 165.59 kPa, IOP: 10–40 mmHg) was more significant than the effect of stretching of the silicone cornea (ΔE = 15.79 kPa, relative elongation: 0.98%–6.49%). Our study sheds light on the potential of using an artificial eye model in OCE research for corneal biomechanics. Furthermore, it is critical to consider the impact of IOP on measurement results when utilizing wave-based OCE in clinical settings for enhanced assessment of corneal biomechanics.

Keywords: Corneal biomechanics; optical coherence elastography; optical coherence tomography; intraocular pressure, mechanical wave propagation

1. Introduction

Corneal biomechanical properties (e.g., stiffness, elasticity, and viscosity) are crucial to maintain the structural stability and visual function of the human eye [1]. Corneal biomechanics—which are affected by normal physiological function, aging, and ocular diseases such as keratoconus [2], glaucoma [3,4], and myopia [5-7]—can also be altered by clinical treatments such as refractive surgery [8-11] and corneal collagen cross-linking [12]. Accordingly, the assessment of corneal biomechanics in a clinical setting would be beneficial in identifying degenerative corneal conditions [13,14], screening refractive surgery candidates [15,16], and evaluating treatment outcomes [17]. However, it remains a long-standing challenge and an active area of research to measure corneal biomechanical properties *in vivo* [1].

Optical coherence elastography (OCE) is a novel elastic imaging technique that quantifies soft tissue biomechanics using a high-resolution optical coherence tomography (OCT) system to detect the tissue response (e.g., displacements or mechanical waves)

under a loading force [18]. Due to the successful implementation of OCT systems in ophthalmology, OCE has been recognized as having great potential in the clinical evaluation of corneal biomechanics, and its development has accelerated over the past decades [19]. Various types of tissue stimulation methods, including mechanical contact [20-22], audio sound [23], pulsed laser [24], air puff/pulse [25,26], and heartbeat stimulation methods [27], have been developed for OCE applications. Among them, the microliter-volume air-pulse simulation method [25] is recognized as a safe and comfortable method for *in vivo* ocular tissue stimulation due to its non-contact, transient (e.g., as short as ~1 ms), low pressure (e.g., < 60 Pa), and highly localized (e.g., 150 μm stimulation diameter) features. Such stimulation approaches generate micrometer to sub-micrometer tissue displacements, which require a high-resolution OCT system to identify the tissue dynamic response. Structural OCT/OCE uses the amplitude of the complex signals to offer micrometer-scale axial and lateral resolutions. Phase-sensitive OCT/OCE employs the phase signals to further enhance the dynamic elastography detection sensitivity to a sub-nanometer scale [28], which allows for the detection of minute-magnitude dynamics in human corneas *in vivo* [20,29,30]. The primary indicator of the tissue's mechanical property is Young's modulus, a representation of elasticity expressed as the slope between the force (stress) and the resulting fractional deformation (strain). The prevalent OCE technique, similar to ultrasonic elastography, works by inducing mechanical waves in the tissue, tracking the wave propagation, and then estimating Young's modulus of the tissue based on the wave velocity [19,31,32]. In general, mechanical waves propagate faster in stiffer materials and slower in softer materials. Reliable measurement of the stimulation-induced mechanical waves for *in vivo* cornea is the top priority for corneal biomechanical property reconstruction using an OCE system [33], but it remains a challenging task [19].

To date, only a few recent pioneering studies have successfully measured the mechanical wave propagations in human corneas *in vivo* [20,29,30]. Ramier et al. [20]evaluated the shear modulus of human corneas by utilizing an OCE system equipped with a vibrational contact probe (diameter: 2 mm) driven by a pair of acoustic transducers (20 mN, frequency: 2–16 kHz). In their study, they measured the Rayleigh-wave speed in 12 healthy individuals (age: 25–67 years, seven males and five females, intraocular pressure [IOP]: 13–18 mmHg) to be 7.86 ± 0.75 m/s. However, they did not identify a correlation between the wave speed and IOP or central corneal thickness [20]. Lan et al. [30] utilized a combination of high-resolution common-path OCT imaging and micro-liter air-pulse stimulation at a pressure of 13 Pa to induce a submicron displacement amplitude on the corneal surface. They observed and measured the propagation of surface waves in the spatio-temporal domain of 18 eyes from nine healthy individuals (three females and six males) with an average age of 27 ± 5 years and an IOP ranging from 9.3–23.2 mmHg. The group velocity of the surface waves ranged from 2.4–4.2 m/s, with a mean of 3.5 m/s, and a 95% confidence interval of 3.2–3.8 m/s. The results showed a correlation between group velocity and central corneal thickness ($r = 0.64$, $P < 0.001$) and IOP ($r = 0.52$, $P = 0.02$) [30].

However, the *in vivo* corneal mechanical wave measurements showed discrepancies in these two pioneering OCE studies [20,30]. The wave propagation speeds in Reference [20] were measured at 7.86 ± 0.75 m/s compared to the 2.4–4.2 m/s reported in Reference [30]. The difference in wave propagation speeds could be attributed to the nonlinear elasticity of the cornea, which varies across different stress-strain regions [1]. Furthermore, the relationship between the mechanical wave speeds and the factors of IOP remains a subject of debate. While Reference [20] found no correlations, Reference [30] found moderate correlations. The controversial results [20,30] may have also resulted from the challenges of *in vivo* corneal wave propagation measurement [1]. Physiological ocular motions (e.g., induced by respiration and heartbeat) can lead to measurement variability for *in vivo* corneal shear waves [34]. The fluctuating IOP values throughout cardiac cycles may affect the testing conditions or alter the corneal biomechanical properties, hence causing measurement discrepancies over time [35]. Additionally, the correlation study between shear

 doi:10.20944/preprints202304.0924.v1

wave velocity and IOP was performed among different eyes; however, it should be noted that each eye has its own features, including different elasticity, viscosity, and geometry (e.g., corneal central thickness, CCT). Previous *in vivo* OCE studies [20,29,30,36,37] have not controlled for individual differences in corneal elasticity, viscosity, and geometry (e.g., central corneal thickness), all of which may affect the *in vivo* OCE measurement results. Therefore, it is possible that these factors contributed to the discrepancies observed among different eyes in the correlation study between shear wave velocity and IOP [20,30].

To investigate the relationship between IOP and mechanical wave propagation under a better-controlled condition, we built an artificial eye model and utilized a microliter air-pulse OCE system to measure the surface wave propagations in the radial directions of the artificial eye's silicone cornea. During OCE measurement, the IOP was increased from 10 mmHg to 40 mmHg by altering the amount of water in the eye model and was monitored by a pressure sensor. The effects of stretching on the elasticity and curvature of silicone corneas were taken into account when calibrating the OCE measurement results. The change in Young's modulus caused by the stretching of the silicone cornea was evaluated independently by mechanical testing of the silicone material, while the change in corneal curvature at each intraocular pressure was acquired by OCT imaging. We aimed to conduct a more robust comparative analysis of the relationship between surface wave propagation speed and the estimated Young's modulus with changes in IOP levels.

2. Materials and Methods

2.1. Artificial Eye Model

Figure 1 illustrates the process to produce the silicone cornea and the whole artificial eye model. In the production of silicone cornea for an artificial eye model, two types of self-defoaming silica gels were used (A silicone and B silicone from Sanjing Xinde Technology Inc, Beijing, China). These two materials were mixed in equal proportions in a petri dish (Figure 1a) and settled for 30 min until all air bubbles had dissipated. The resulting silicone mixture was poured into a corneal mold that had been previously coated with a petroleum jelly layer to prevent adherence (Figure 1b). A cap was placed on top of the mold to form the silicone into a desired shape. The mold was then placed in a refrigerator for 1 day to ensure complete solidification of the silicone. The silicone cornea was then removed from the mold, as depicted in Figure 1c. The rest of the artificial eye model was 3D-printed, featuring a cover and a chamber that sandwiched the silicone cornea's edge (Figure 1d). The chamber has two channels, which can further link to a water tube and a pressor sensor for controlling IOP (also see Figure 2b).

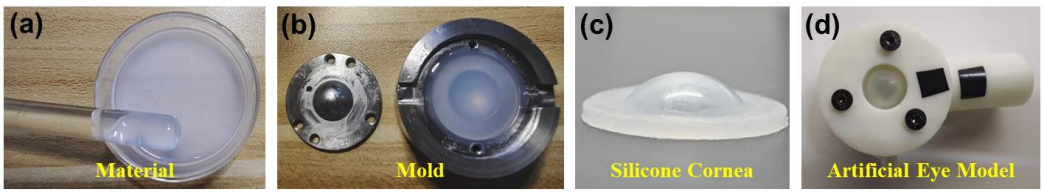

Figure 1. Demonstration of the production process for the artificial eye model. (a–c) Production of the silicone cornea using the mold. (d) The silicone cornea is sandwiched by a cover and a camber to form the artificial eye model. The chamber has two channels, which can further link to a water tube and a pressor sensor (also see Figure 2b).

2.2. OCE System Set-Up

A detailed description of this OCE system has been provided in our previous work [38,39]. In summary, this OCE system was built by combining a microliter air-pulse mechanical stimulation system and a 1290–nm linear-wavenumber (k) spectral domain OCT platform [40] (Figure 1a). Microliter air-pulses (99.99% nitrogen) were delivered to the silicone corneal apex of the artificial eye model via a microbore cannula controlled by a

Preprints (www.preprints.org) | NOT PEER-REVIEWED | Posted: 25 April 2023 doi:10.20944/preprints202304.0924.v1

high-speed solenoid valve. The air pulse had a low pressure (~200 Pa), a short duration time (~3 ms), and a small diameter (150 μm). The light source in the OCT system was a superluminescent diode (SLD, IPSDS1307C-1311, Inphenix Inc., Livermore, CA, USA) with a 3-dB bandwidth of 1290 ± 40 nm. The light was split 50:50 to the reference and sample arms. In the sample arm, light was collimated to a 4-mm parallel beam, scanned by 2-dimensional galvo mirrors, and then focused by a 54-mm telecentric scan objective (LSM54-1310, Thorlabs Inc., Newton, NJ, USA) with a wide scan field (18.8 × 18.8 mm^2). The maximum output power was ~1.8 mW measured at the sample surface. The returned light from both arms was interfered and recorded by a linear-wavenumber (k) spectrometer (PSLKS1300–001-GL, Pharostek, Rochester, Minnesota, USA). The combination of the grating and prism (Figure 1a) in the linear-k spectrometer disperses the spectrum linearly in the k domain to improve the signal-to-noise ratio (SNR) in deeper tissue, and to reduce the computing time required to convert the spectrum from the wavelength domain to the wavenumber domain as in a conventional grating-based spectrometer [41,42]. The k-domain interference signals were captured by an InGaAs line scan camera with 2048 pixels and a line rate of 76 kHz (GL2048L-10A-ENC-STD-210, Sensors Unlimited, Inc., Princeton, NJ, USA). The acquired signals were sent to a computer where they were processed via Fourier transform to acquire the depth profiles (A-scans) using code written in the LabVIEW language. The OCT imaging system had a 6.94-mm imaging depth, a 99.3 dB maximum sensitivity, and a maximum sensitivity fall-off of −28.6 dB, with a −6 dB fall-off range of ~0–3 mm. The axial resolution was ~15 μm (all calibrated in air).

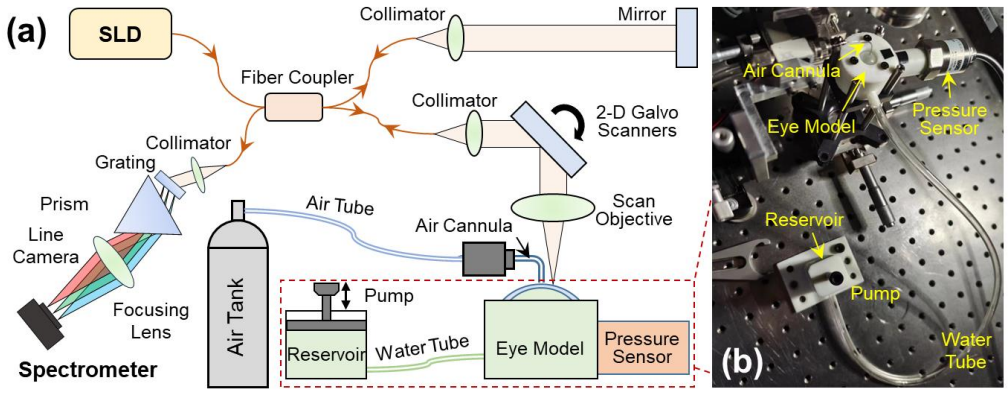

Figure 2. Set-up for the optical coherence elastography (OCE) system and the artificial eye model. (a) A microliter air pulse is used to stimulate the silicone cornea perpendicularly, and a spectrum domain OCT system is used to track the micron-scale surface waves. The SLD is a superluminescent laser diode with a waveband of 1290 ± 40 nm; a linear-wavenumber (k) spectrometer was used to disperse the interference spectrum in the k-domain prior to the Fourier transform for OCT processing. (b) The artificial eye model comprises a silicone cornea and water chamber connected to a chamber connected to two channels, one linked to a water tube and a reservoir to regulate water volume in the chamber, and the other connected to a pressor sensor for monitoring the equivalent IOP inside the chamber.

Figure 2b demonstrates the artificial eye model during OCE measurement. The eye model was connected to two channels, one linked to a water tube and a reservoir to regulate water volume in the chamber, and the other connected to a pressor sensor (WNK81MA, Vanke Electric Xin Engineering Co., Ltd., Anhui, China) for monitoring the chamber pressure (i.e., equivalent IOP). To facilitate OCE mechanical wave measurement, the pressure was controlled in the range of 10 mmHg to 40 mmHg.

2.3. M-B Mode Radial Scan Patten

The OCT system was synchronized to the stimulation to observe and quantify the induced dynamic response in the radial directions surrounding the stimulation point

Preprints (www.preprints.org) | NOT PEER-REVIEWED | Posted: 25 April 2023 doi:10.20944/preprints202304.0924.v1

(corneal apex). Figure 3a shows the OCE measuring geometry between the stimulation and measurement points. The air pulse was delivered at the silicone corneal apex, and the OCE measurement was performed in each radial direction from 54° to 324°. The angle between adjacent radial directions was 18°, and each direction had 17 measurement points to cover a distance of 0.93—2.05 mm. The measurement was performed using an M-B mode scan protocol to measure the surface displacement as a function of time and to track elastic wave propagation through the tissue surface [32]. The air pulse was stimulated every 0.5 s, and the OCE measurement was synchronized to the stimulation and measured 11.4 ms at each point to detect the temporal displacement profile of that point. The surface wave propagation speed can be estimated between the time delay of a certain distance.

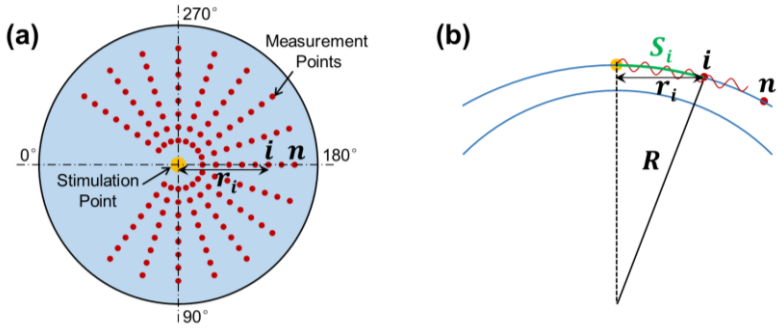

Figure 3. Radial scan pattern for the measurement of surface wave propagation. (a) Stimulation and measurement geometry. Air pulse stimulation was performed at the apex of the silicone cornea, and measurement was performed at each radial direction from 45° to 315°. (b) Surface wave propagation distance (Arc distance: S_i) in response to corneal curvature (R) and radial distance (r_i).

In the complex OCT interferogram signal ($\mathrm{OCT_{complex}}$), the phase signal ϕ can be determined by the real and imaginary parts of the OCT signals as follows:

$$\emptyset = arctan\left[\frac{Im(\mathrm{OCT_{complex}})}{Re(\mathrm{OCT_{complex}})}\right]. \quad (1)$$

The temporal profile of phase variation $\phi(t)$ can usually be resolved and unwrapped by tracing one point in a time sequence (reference to time t_0) among the successive A-scan signals. Surface displacements $y(t)$ can be converted from the phase signals as follows [43]:

$$y(t) = \frac{\lambda_0}{4\pi n}\phi(t), \quad (2)$$

where λ_0 is the center wavelength, and n is the refractive index ($n = 1$ in air). In the absence of applied forces, the phase stability (standard deviation) was measured using a mirror that was 4.3 ± 1.4 milliradians over 60 ms (10 repetitive measurements) in the common-path OCT setup, corresponding to displacements of 0.44 ± 0.14 nm.

In OCE measurement, the mechanical wave propagation velocity is directly correlated with the tissue's mechanical property [44-46]. In general, the wave propagates faster in a stiffer material and slower in a softer material. Young's modulus (E) is a measure of elasticity and is represented as the ratio of stress to strain. A larger value of Young's modulus is associated with greater tissue stiffness, and thus, faster mechanical wave traveling speed during OCE measurement. In a surface wave equation, the relation between the group velocity (c) and Young's modulus can be expressed as follows [47]:

$$E = \frac{2\rho(1+v)^3}{(0.87+1.12v)^2}c^2, \quad (3)$$

 doi:10.20944/preprints202304.0924.v1

where ρ is the density, ν is the Poisson's ratio. Generally, ν can be assumed as 0.49. The group velocity of the elastic surface wave was estimated as follows:

$$c = \frac{1}{n}\sum_{i=1}^{n}\left(\frac{S_i}{t_i}\right), \quad (4)$$

where S_i and t_i represent the traveling distance and time delay for the surface wave to travel from the stimulation point to the measurement point i ($i = 1, \ldots, n$), respectively. When the stimulation was on the corneal apex, the traveling distance S_i along the corneal surface (arc distance) is

$$S_i = R \cdot \arctan\left(\frac{r_i}{R}\right), \quad (5)$$

where r_i is the OCT scan (or horizontal) distance, and R is the radius of curvature for the anterior cornea (See Figure 3b). Equation 4 can typically be accomplished using linear curve fitting [30].

3. Results

3.1. Geometry of the Silicone Cornea in Association with IOP Values

As the pressure within the artificial eye model increases, the silicone cornea is subject to stretching and protrusion, resulting in changes to its radius of curvature and thickness, which can affect the OCE measurement results. To account for this, the structure of the silicone cornea was calibrated at different IOPs, ranging from 0–40 mmHg, as shown in Figure 4. The refractive indexes of the silicone and water were measured as 1.496 and 1.371, respectively, at the wavelength of 1290 nm. Figure 4(a–e) displays cross-sectional OCT images of the silicone cornea at different IOPs, with Figure 4a showing the relaxation condition (0 mmHg), and Figure 4(b–e) showing the pre-stress condition loaded by water pressure (10–40 mmHg). The silicone corneal diameter (SCD) was 11.76 mm, and the anterior surface depth (ASD), radius of curvature (R), central corneal thickness (CCT), and anterior surface length (ASL) were measured as the IOP increased from 0 mmHg to 40 mmHg (Figure 4(f–i)). In Figure 4f, the ASD values were measured between the corneal apex and boundary and observed to increase from 2.73 to 3.30 mm (linear fitting equation: y = 0.0142x + 2.726, R^2 = 0.999) as the IOP increased. The R of the equivalent spherical anterior surface was calculated using $R = (4ASD^2 + SCD^2)/8ASD$, and was observed to decrease from 7.70 mm to 6.89 mm (linear fitting equation: y = −0.0202x + 7.678, R^2 = 0.996, Figure 4g). The CCT decreased from 0.545 mm to 0.477 mm (linear fitting equation: y = −1.772x + 551.6, R^2 = 0.968, Figure 4h) with increasing IOP. Furthermore, the ASL was observed to elongate from 14.59 mm to 15.64 mm (linear fitting equation: y = 0.0238x + 14.53, R2 = 0.983, Figure 4i). The calibrated ASL values can be used to estimate changes in the cornea's mechanical properties (i.e., Young's modulus) through mechanical testing (see Section 3.2).

Preprints (www.preprints.org) | NOT PEER-REVIEWED | Posted: 25 April 2023 doi:10.20944/preprints202304.0924.v1

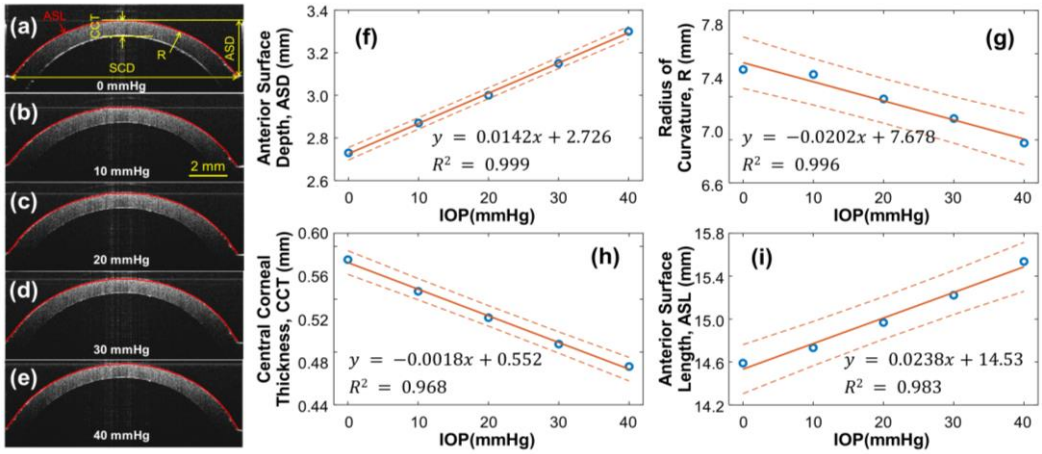

Figure 4. Silicone cornea geometry calibration under 0–40 mmHg IOPs. (a–e) Silicon cornea OCT imaging at various IOP levels. The anterior surface is segmented for cornea geometry calculation. SCD: Silicone corneal diameter. (f–i) IOP-dependent anterior surface depth (ASD), radius of curvature (R), central corneal thickness (CCT), and anterior surface length (ASL).

As the R varied depending on the IOP values, the arc distance along the anterior surface of the silicone cornea between the stimulation point and each measurement point (as illustrated in Figure 3b) also changed. We used the arc distance as the wave propagation distance for the surface wave speed calculation (Equations 4 and 5). The OCT line scan distance in each radial direction was 0.933–2.053 mm, and the measured arc distances in each radial direction were 0.960–2.519 mm (10 mmHg), 1.018–2.671 mm (20 mmHg), 1.067–2.801 mm (30 mmHg), and 1.130–2.964 mm (40 mmHg), as shown in Figure 5.

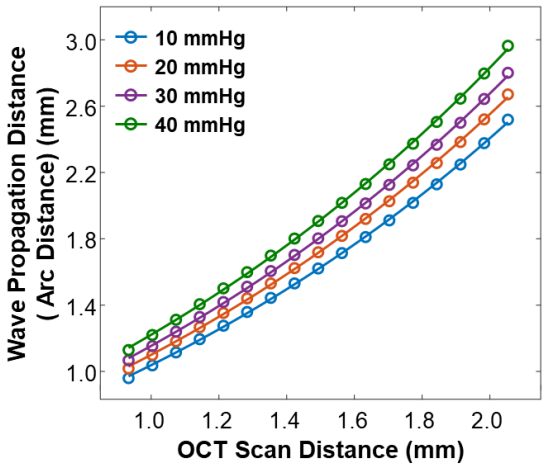

Figure 5. Calibration between the OCT line scan distance and the arc distance of the silicone cornea at various IOP values from 10 mmHg to 40 mmHg.

3.2. Effect of Stretching on Young's Modulus of Silicone Material

When the water pressure inside the artificial eye model (equivalent to the IOP) increased, the silicone cornea protruded forward, stretching the silicone cornea along radial directions, which caused a change in the elasticity of the silicone material (Figure 6a). To emulate the stretching condition of the silicone cornea caused by increased IOP, we conducted mechanical testing on a silicone block to measure the change in Young's modulus when the material was stretched, as shown in Figure 5(b–f). The measurement was repeated five times. A cylindrical silicone block with a natural diameter of D_0 = 44.00 mm, and thickness of H_0 = 10.58 mm was fixed with eight posts and stretched radially by two positioning discs, as illustrated in Figure 5(b–d). The outer diameter of the positioning

Preprints (www.preprints.org) | NOT PEER-REVIEWED | Posted: 25 April 2023 doi:10.20944/preprints202304.0924.v1

discs determined the stretched value (ΔD), while the central area of the silicone material was placed between two plates on the top and below for compression testing. As the diameter of the cylindrical silicone block was stretched from 44.00 mm (D_0) to 56.00 mm (increase step: 2 mm, maximum ΔD = 12 mm), the center thickness H was reduced from 10.85 $\pm$ 0.05 mm (H_0) to 9.04 $\pm$ 0.06 mm (linear fitting: $y = -0.14x + 17.10$, $R^2 = 0.995$, Figure 6e). The measured Young's modulus of the stretched silicone block was increased from 1001.1 ± 14.64 kPa (E_0) to 1580.3 ± 50.58 kPa (maximum ΔE = 579.2 kPa, maximum $\Delta E/E_0$ = 57.86%). As shown in Figure 6f, the correlation between the relative change in Young's modulus ($\Delta E/E_0$) and the relative diameter elongation value ($\Delta D/D_0$: 0%–27.27%) was as follows:

$$\frac{\Delta E}{E_0} = 1.973\frac{\Delta D}{D_0}, \quad (6)$$

where the fitting $R^2 = 0.981$. Equation 6 can be used to predict the trend of Young's modulus change in response to the stretching effect and can be used to calibrate the OCE measurement results on Young's modulus estimation and correlation study between Young's modulus and IOP (Section 3.3, Figure 9).

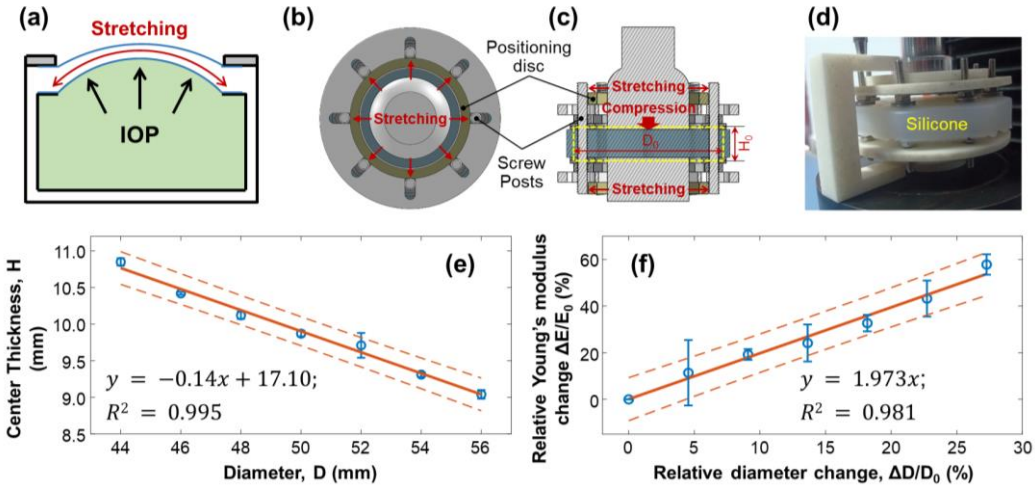

Figure 6. Mechanical testing of silicone material to replicate the change in Young's modulus due to stretching. (a) The cornea of an artificial eye model protrudes forwards under water pressure, leading to pre-stress conditions along the radial directions of the silicone cornea. The increase in Young's modulus of the silicone material was estimated in panels (b–f). Panels (b, c, and d) show the top view, sectional view, and photo imaging of the testing conditions, where a cylindrical silicone block (diameter: D; thickness: H) was fixed with eight posts and stretched radially by two positioning discs positioned on top and below the testing material. The outer diameters of the positioning discs controlled the stretched value (ΔD), while the central area of the silicone material was placed between a compressor on top and a metal plate below, both of which had a diameter of 30 mm. (e) The diameter was stretched from 44 mm (D_0) to 56 mm (maximum ΔD = 12 mm), reducing the center thickness from 10.85 mm to 9.04 mm. (f) The correlation between the relative change in Young's modulus ($\Delta E/E_0$) and the relative diameter elongation value ($\Delta D/D_0$: 0–27.27%) shows an increase in Young's modulus (maximum $\Delta E/E_0$ = 57.86%, five repeat measurements).

3.3. Surface Wave Characterization in the Silicone Cornea

The speed of surface waves was determined by measuring the distance and time delay between the stimulation and measurement points (Equations 4 and 5). Figure 7 provides an example of this calculation for the silicone cornea at 10 mmHg IOP in the 180° direction (as shown in Figure 3a). The measurement was repeated 10 times. The surface displacement profiles in the temporal and tempo-spatial domains are depicted in Figures 7(a, b). The stimulation was applied at the cornea apex, and measurements were taken at 17 sampling points along a scanning distance of 0.933 mm–2.053 mm, covering an arc

Preprints (www.preprints.org) | NOT PEER-REVIEWED | Posted: 25 April 2023 doi:10.20944/preprints202304.0924.v1

distance of 0.960–2.519 mm along the surface of the silicone cornea. The induced surface dynamics exhibited three periods [28]: (1) a baseline period before stimulation; (2) a stimulation-force-driven primary deformation period where displacement increased from baseline to the maximum negative displacement and then recovered; and (3) a vibration period, which underwent a decay oscillation and returned gradually to its baseline position. The maximum negative displacement amplitude (A_0) of each measurement location within the analysis window (4.0–6.8 ms) was assessed to characterize the mechanical wave propagation. Figure 7c shows the decay of A_0 during wave propagation. In this study, the amplitude decreased from -3.50 ± 0.05 μm to -1.38 ± 0.02 μm as the measurement arc distance increased from 0.960–2.519 mm. An exponential function can be used to describe the distance-dependent decay of the primary deformation [48]. The curve was fitted as $y = A_0 e^{B(x-0.96)}$, where A_0 is the amplitude, B is the decay coefficient, and the x and y-axis scales are in millimeters and micrometers, respectively. The obtained values were $A_0 = -3.56\ \mu m, B = -0.57\ mm^{-1}, and\ R^2 = 0.978$. Figure 7d shows a linear fitting between the time delay and measurement position, and the slope of this curve represents the wave propagation speed along the 180° direction of the silicone cornea at 10 mmHg IOP. The observed wave propagation speed was 6.48 m/s (95% CI: 6.47–6.49, $R^2 = 0.98$).

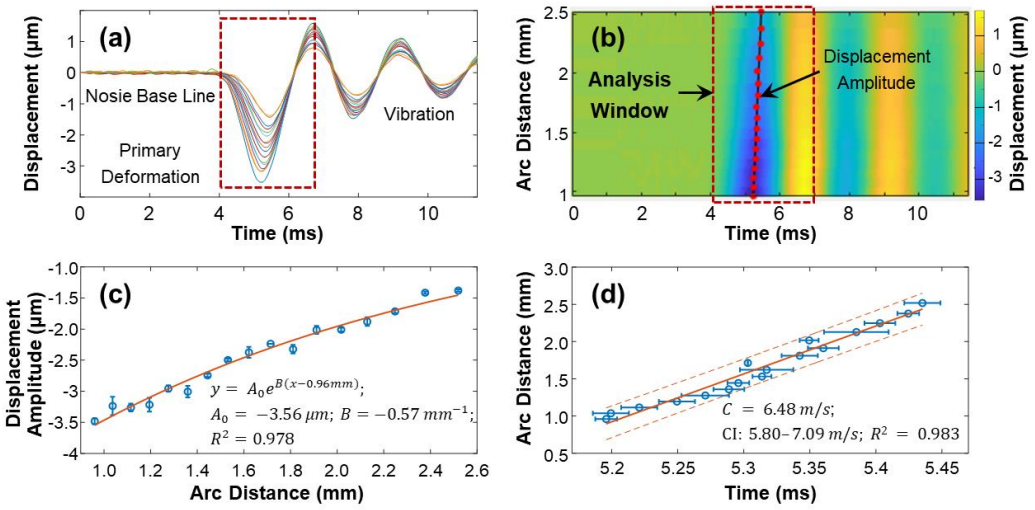

Figure 7. Demonstration of the surface wave speed quantification method for the silicon cornea (10 mmHg) at the 180° direction. (a) Surface displacement in the temporal domain. Color series: 17 measurement points at an OCT scan distance of 0.933–2.053 mm, covering an arc distance of 0.960–2.519 mm. (b) Tempo-spatial map of the surface wave propagation. The displacement magnitudes were used for magnitude decay fitting in (c) and mechanical wave propagation speed fitting in (d) by 10 time repeat measurements.

Figure 8 illustrates the propagation of surface waves in the radial directions (54° to 324°) of the silicone cornea at an IOP of 10 mmHg. Figure 8a shows the propagation and attenuation process of the surface wave at varying measurement points on the silicone corneal surface (top view) during different OCE measurement times (4–9 ms). Because the silicone cornea was fabricated uniformly in its radial directions, the propagation waves also presented a uniform geometry surrounding the stimulation point (apex of the silicone cornea). The propagation feature of surface waves is fully illustrated in Video S1, which can be found in the supplementary materials. Figure 8b illustrates the tempo-spatial relation of the surface wave in five propagation directions (90°, 126°, 180°, 234°, and 270°), with velocities ranging from 6.48 ± 0.15 m/s to 6.67 ± 0.31 m/s. Notably, the surface waves propagate consistently with similar displacement magnitudes and propagation speeds in all radial directions in the isotropic samples, as demonstrated in this example.

Preprints (www.preprints.org) | NOT PEER-REVIEWED | Posted: 25 April 2023 doi:10.20944/preprints202304.0924.v1

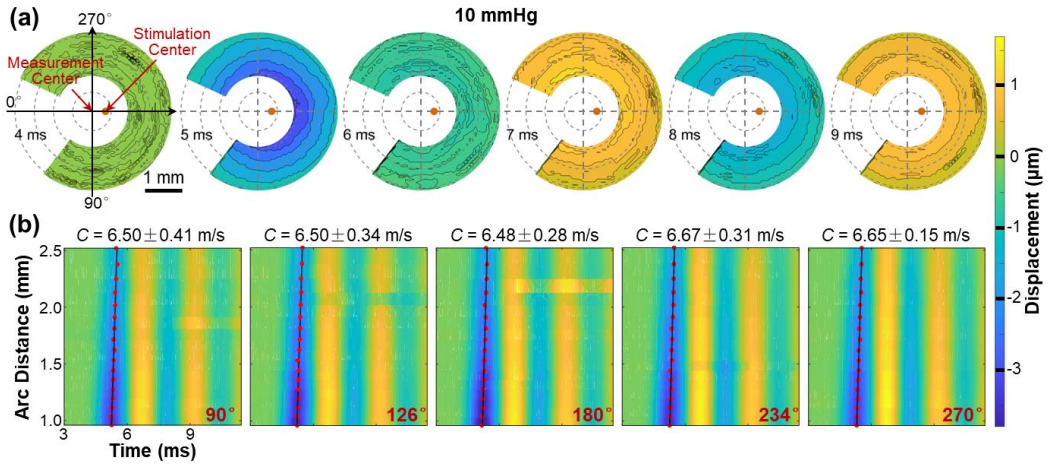

Figure 8. Surface wave propagation in the radial directions (54° to 324°) of the silicone cornea (IOP: 10 mmHg). See **Video S1** in Supplementary Materials. (a) *En face* surface wave profiles at different times from 4 ms to 9 ms. (b) Tempo-spatial profiles of the surface wave propagation at five selected directions. The wave propagation speeds were calculated by linear-fitting for the maximum displacement amplitudes.

Figure 9 illustrates the characteristics of surface wave propagation and the estimated Young's modulus in the radial directions (54° to 324°) of the silicone cornea at IOPs ranging from 10 mmHg to 40 mmHg. The experiment was repeated 10 times. In Figure 9a, the wave propagation speeds (mean ± fitting confident intervals) are presented in different directions and at various IOPs. The waves propagated uniformly in each radial direction with speeds (mean ± STD) of 6.55 ± 0.09 m/s (10 mmHg), 7.06 ± 0.10 m/s (20 mmHg), 7.72 ± 0.07 m/s (30 mmHg), and 9.82 ± 0.19 (40 mmHg). Figure 9b shows the primary magnitude (A_0) of the displacements. An offset between the measurement center and stimulation center was observed. The displacements distribute evenly surrounding the stimulation center, with measurements of 3.13 ± 0.27 μm (10 mmHg), 2.68 ± 0.22 μm (20 mmHg), 2.29 ± 0.15 μm (30 mmHg), and 2.13 ± 0.15 μm (40 mmHg). Figure 9c shows the correlation between the surface wave speeds and the IOPs (exponential fitting: $y = 0.24e^{0.09(x-10)} + 6.37$, $R^2 = 0.997$). Figure 9d shows the measured and calibrated Young's modulus (in kPa) in association with the IOPs (in mmHg). The solid blue line displays Young's moduli estimated using the surface wave speeds, which were 145.23 ± 4.43 kPa (10 mmHg), 168.73 ± 4.78 kPa (20 mmHg), 201.75 ± 3.66 kPa (30 mmHg), and 326.44 ± 13.30 kPa (40 mmHg). The correlation between the wave-based Young's moduli and IOP was fitted as an exponential curve, $y = 19.45e^{0.1072(x-10)} + 141.3$, $R^2 = 0.992$. The dashed green line represents the stretching effect of the silicone material on Young's modulus change using Equation 6. Predicted linear increments of stretching-induced Young's moduli ranged from 145.23 kPa (10 mmHg) to 161.02 kPa (40 mmHg), as the relative anterior surface length varied from 0.98% (10 mmHg) to 6.49% (40 mmHg). Furthermore, the orange line in Figure 9d depicts Young's modulus relative to the IOP change after the stretching effect was removed, which was 145.23 kPa (10 mmHg), 164.17 kPa (20 mmHg), 192.23 kPa (30 mmHg), and 310.82 kPa (40 mmHg). The correlation between the calibrated Young's moduli and IOP was $y = 13.71e^{0.119(x-10)} + 143.7$, $R^2 = 0.998$.

Based on the findings, there is a relationship between mechanical wave speeds, corneal mechanical properties, and IOP. In this artificial eye model study, the stretching effect had a minimal impact on Young's modulus (ΔE = 15.79 kPa, from 10–40 mmHg), while the IOP significantly affected the mechanical wave propagation speed and the resulting estimations of Young's modulus (ΔE = 165.59 kPa, from 10–40 mmHg). Consequently, when applying the wave-based OCE to clinical settings, it is critical to address the impact of IOP on the measurement results for a more accurate assessment of corneal biomechanics.

Preprints (www.preprints.org) | NOT PEER-REVIEWED | Posted: 25 April 2023 doi:10.20944/preprints202304.0924.v1

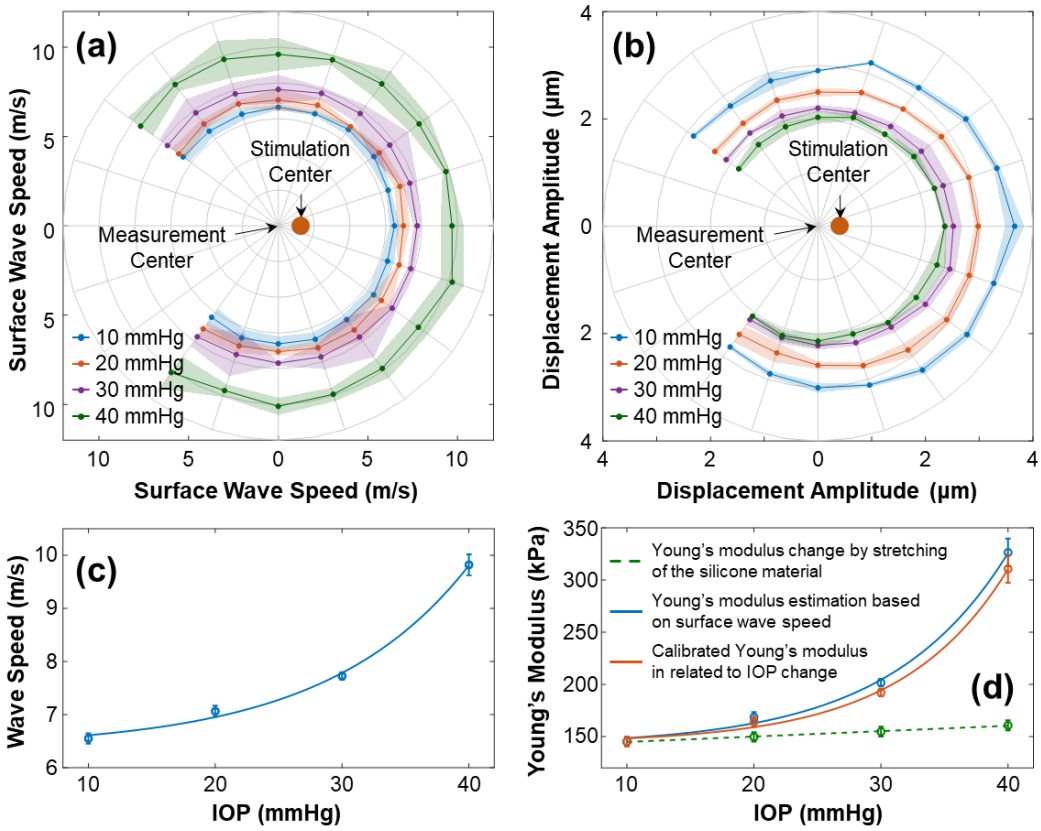

Figure 9. Characterization of the surface wave and Young's modulus for the silicone cornea at different IOPs from 10–40 mmHg. The measurements were repeated 10 times. (a) and (b) Show directional-dependent wave propagation speeds and displacement amplitudes (A_0) for 54–324° angles of the silicone cornea at varying IOP levels. (c) Illustrates the mean ± STD of surface wave propagation speeds associated with different IOPs. (d) Shows the measured and calibrated Young's moduli (mean ± STD) in association with IOPs. The dashed green line depicts the trend of Young's modulus increase caused by material stretching (Equation 6). The solid blue line shows the estimated Young's moduli using surface wave speed in (c) and Equation (3), while the orange line shows the calibrated Young's modulus relative to the IOP change.

4. Discussion and Conclusions

The relationship between mechanical wave speeds and IOP levels remains a topic of debate [20,30] due to the difficulties in conducting *in vivo* corneal OCE measurements. To gain a better understanding of this, we constructed an artificial eye model and utilized a microliter air-pulse OCE system to measure the surface wave propagations in the radial directions of the silicone cornea. Employing an artificial eye model offers several benefits, including a simplified and controlled measurement condition with adjustable and monitorable IOP values, as well as the removal of the physiological ocular motions typically induced by respiration and heartbeat. Additionally, using silicone material in the model eliminates the complex mechanical properties found in the corneal tissue, which can be viscous, anisotropic, and highly nonlinear in response to stress and strain.

During OCE measurement, the IOP increased from 10 mmHg to 40 mmHg by altering the amount of water in the eye model and was monitored by a pressure sensor. As the pressure increased, the silicone cornea stretched further and protruded forward, causing a decrease in its radius of curvature and thickness, both of which can affect OCE measurement outcomes. To account for these changes, we calibrated the OCE surface wave measurement results using two methods. First, we measured the cornea's geometry parameters using OCT imaging to calibrate surface wave velocity (refer to Figure 4 and Figure 5). Second, we evaluated Young's modulus change in the silicone material due to its

 doi:10.20944/preprints202304.0924.v1

elongation using a mechanical testing method (Equation 6). Applying these calibration techniques helped to obtain accurate OCE measurement results while accounting for the changes in geometry and elasticity of the silicone cornea due to water pressure.

As illustrated in Figure 9, the surface wave propagated evenly in the radial directions of the silicone cornea, along a scanning distance of 0.933 mm–2.053 mm (arc distance: from 0.960–2.519 mm at 10 mmHg to 1.130–2.964 mm at 40 mmHg). The measured surface wave velocity increased from 6.55 ± 0.09 m/s to 9.82 ± 0.19 m/s as the IOP increased from 10 to 40 mmHg, resulting in an estimate of Young's modulus, which increased exponentially from 145.23 ± 4.43 kPa to 326.44 ± 13.30 kPa. As the elongation of the silicone material changes Young's modulus linearly (ΔE = 15.79 kPa, relative elongation: 0.98%–6.49%), the calibrated Young's modulus, after accounting for the effect of elongation, still exhibits an exponential trend (ΔE = 165.59 kPa, IOP: 10–40 mmHg). As a result, the stretching has a relatively small impact on Young's modulus of the cornea. The mechanical wave propagation speed of the cornea is more significantly affected by IOP. Thereby, further studies should be performed to better separate the effect of IOP on Young's modulus estimation in wave-based corneal OCE application.

This study has certain limitations that may impact the estimation accuracy of the correlation between surface wave speeds and IOPs. First, the use of a single-layered silicone cornea may not fully replicate the behavior of the human eye as IOPs increase. The human cornea is a complex, layered structure with varying stiffnesses in different regions and directions. The stroma, which comprises the majority of the cornea's thickness, largely determines the overall properties of the human cornea. The orientation and depth-arranged pattern of the collagen fibers/lamellae of the stroma result in the anterior portion of the cornea having the most strength, followed by the middle part, while the posterior part is the softest. As a result, the human cornea can uniquely adapt to fluctuations in IOP. Specifically, the inner section of the cornea can change its geometry to accommodate these changes, while the outer layer of the cornea can maintain its shape and preserve the quality of vision. However, this is not the case for OCE measurements of the silicone cornea in artificial eye models, where the entire silicone cornea changes shape and thickness in response to changes in IOP. Although calibration has been performed to account for changes in corneal shape and elasticity due to pre-stress conditions caused by IOP, this calibration may not fully reflect the actual situation. Future studies should focus on developing multi-layered silicone corneas that accurately represent the axial distribution of corneal mechanical properties to better simulate the behavior of the eye when the IOP changes. Furthermore, the mechanical calibration methods may only partially represent the actual elasticity changes of the silicone cornea at various IOP levels. Soft materials, such as the cornea and silicone, typically exhibit non-linear elasticity, which means that the estimated Young's modulus is lower in the low strain region (e.g., hundreds of kPa in microliter air-pulse OCE measurement, as illustrated in Figure 9), but higher in the high strain region (~MPa, as demonstrated in Figure 6, in mechanical testing). Consequently, the linear estimation in Equation 6 between the relative change in Young's modulus ($\Delta E/E$) and the elongation rate ($\Delta D/D$) could overestimate the trend of Young's modulus change when the silicone material is stretched in a low value. Nevertheless, it is important to note that even if the increase in Young's modulus due to stretching is overestimated, its overall impact on Young's modulus is relatively small. As a result, the effect of IOP on the corneal mechanical wave speed, as well as the estimated Young's modulus, far outweighs the increase in Young's modulus due to the stretching of the silicone material.

Our study sheds light on the potential of using artificial eye models in OCE research for corneal biomechanics, allowing for greater control and accuracy in studying the relationship between mechanical wave propagation and IOP changes. Through the implementation of an artificial eye model, we discovered that the impact of IOP on corneal mechanical wave propagation (and Young's modulus estimation) is more significant than the effect of stretching of the silicone cornea when using the wave-based OCE measurement. Therefore, in translating the wave-based OCE to clinical applications, it is crucial to pay

close attention to how to remove the influence of IOP to evaluate its Young's modulus. With the continuous advancement of OCE technology and methodologies, the understanding of corneal biomechanics will be further improved, facilitating enhanced diagnosis and treatment of ocular diseases.

Supplementary Materials: The following supporting information can be downloaded at: www.mdpi.com/xxx/s1, Video S1: Surface wave propagation.

Author Contributions: Conceptualization: GL and GM; Methodology: GL, JF and GM; Software: GM, HY, JC, RZ, WH, and CS; Validation: CD and MDT; Formal analysis: GL, GM and CS; Investigation: GL; Resources: GL, LA, JQ, YH and JX; Data curation: GM and GL; Writing—original draft preparation: GL and GM; writing—review and editing: All authors; Visualization: GM and GL; Supervision: GL; Project administration: JC; Funding acquisition: GL, LA, MDT.

Funding: National Natural Science Foundation of China (61975030); Guangdong Basic and Applied Basic Research Foundation (2021A1515011981); Innovation and Entrepreneurship Teams Project of Guangdong Pearl River Talents Program (2019ZT08Y105); Guangdong-Hong Kong-Macao Intelligent Micro-Nano Optoelectronic Technology Joint Laboratory (2020B1212030010); National Institutes of Health/National Eye Institute (NIH/NEI) P30EY07551, R01EY022362, and R01EY022362.

Institutional Review Board Statement: Not applicable.

Informed Consent Statement: Not applicable.
Data Availability Statement: The original contributions presented in the study are included in the article/Supplementary Material, further inquiries can be directed to the corresponding authors.

Acknowledgments: In this section, you can acknowledge any support given which is not covered by the author contribution or funding sections. This may include administrative and technical support, or donations in kind (e.g., materials used for experiments).

Conflicts of Interest: GL, YH, and JX are consultants at Weiren Meditech Co., Ltd. JQ and LA are currently working at Weiren Meditech Co., Ltd. Remaining authors have no disclosures. The funders had no role in the design of the study; in the collection, analyses, or interpretation of data; in the writing of the manuscript; or in the decision to publish the results.

References

1. Lan, G.; Twa, M.D.; Song, C.; Feng, J.; Huang, Y.; Xu, J.; Qin, J.; An, L.; Wei, X. In Vivo Corneal Elastography: A Topical Review of Challenges and Opportunities. *Computational and Structural Biotechnology Journal* **2023**, doi:https://doi.org/10.1016/j.csbj.2023.04.009.
2. Wolffsohn, J.S.; Safeen, S.; Shah, S.; Laiquzzaman, M. Changes of corneal biomechanics with keratoconus. *Cornea* **2012**, *31*, 849-854, doi: 10.1097/ICO.0b013e318243e42d.
3. Jonas, J.B.; Aung, T.; Bourne, R.R.; Bron, A.M.; Ritch, R.; Panda-Jonas, S. Glaucoma. *Lancet* **2017**, *390*, 2183-2193, doi:10.1016/S0140-6736(17)31469-1.
4. Brown, K.E.; Congdon, N.G. Corneal structure and biomechanics: impact on the diagnosis and management of glaucoma. *Curr. Opin. Ophthalmol.* **2006**, *17*, 338-343, doi:10.1097/01.icu.0000233951.01971.5b
5. Resnikoff, S.; Pascolini, D.; Mariotti, S.P.; Pokharel, G.P. Global magnitude of visual impairment caused by uncorrected refractive errors in 2004. *Bull. World Health Organ.* **2008**, *86*, 63-70, doi:10.2471/blt.07.041210
6. Shen, M.; Fan, F.; Xue, A.; Wang, J.; Zhou, X.; Lu, F. Biomechanical properties of the cornea in high myopia. *Vision Res.* **2008**, *48*, 2167-2171, doi:10.1016/j.visres.2008.06.020
7. Chansangpetch, S.; Panpruk, R.; Manassakorn, A.; Tantisevi, V.; Rojanapongpun, P.; Hurst, C.P.; Lin, S.C. Impact of myopia on corneal biomechanics in glaucoma and nonglaucoma patients. *Invest. Ophthalmol. Vis. Sci.* **2017**, *58*, 4990-4996, doi:10.1167/iovs.17-22219
8. Kim, T.I.; Alió Del Barrio, J.L.; Wilkins, M.; Cochener, B.; Ang, M. Refractive surgery. *Lancet* **2019**, *393*, 2085-2098, doi:10.1016/s0140-6736(18)33209-4.

9. Guo, H.; Hosseini-Moghaddam, S.M.; Hodge, W. Corneal biomechanical properties after SMILE versus FLEX, LASIK, LASEK, or PRK: a systematic review and meta-analysis. *BMC ophthalmol.* **2019**, *19*, 1-20, doi: 10.1186/s12886-019-1165-3.
10. Wang, D.; Liu, M.; Chen, Y.; Zhang, X.; Xu, Y.; Wang, J.; To, C.-h.; Liu, Q. Differences in the corneal biomechanical changes after SMILE and LASIK. *J. Refract. Surg.* **2014**, *30*, 702-707, doi:10.3928/1081597X-20140903-09.
11. Shetty, R.; Francis, M.; Shroff, R.; Pahuja, N.; Khamar, P.; Girrish, M.; Nuijts, R.M.; Roy, A.S. Corneal biomechanical changes and tissue remodeling after SMILE and LASIK. *Invest. Ophthalmol. Vis. Sci.* **2017**, *58*, 5703-5712, doi:10.1167/iovs.17-22864
12. Hammer, A.; Richoz, O.; Mosquera, S.A.; Tabibian, D.; Hoogewoud, F.; Hafezi, F. Corneal biomechanical properties at different corneal cross-linking (CXL) irradiances. *Invest. Ophthalmol. Vis. Sci.* **2014**, *55*, 2881-2884, doi:10.1167/iovs.13-13748
13. Scarcelli, G.; Besner, S.; Pineda, R.; Yun, S.H.; science, v. Biomechanical characterization of keratoconus corneas ex vivo with Brillouin microscopy. *Invest. Ophthalmol. Vis. Sci.* **2014**, *55*, 4490-4495, doi:10.1167/iovs.14-14450.
14. Shah, S.; Laiquzzaman, M.; Bhojwani, R.; Mantry, S.; Cunliffe, I. Assessment of the biomechanical properties of the cornea with the ocular response analyzer in normal and keratoconic eyes. *Invest. Ophthalmol. Vis. Sci.* **2007**, *48*, 3026-3031, doi:10.1167/iovs.04-0694.
15. Kanellopoulos, A.J. Post-LASIK ectasia. *Ophthalmology* **2007**, *114*, 1230-1230, doi:DOI: 10.1016/j.ophtha.2007.03.041.
16. Binder, P.S.; Lindstrom, R.L.; Stulting, R.D.; Donnenfeld, E.; Wu, H.; McDonnell, P.; Rabinowitz, Y. Keratoconus and corneal ectasia after LASIK. *J. Refract. Surg.* **2005**, *21*, 749-752, doi:10.3928/1081-597X-20051101-15
17. Seven, I.; Vahdati, A.; De Stefano, V.S.; Krueger, R.R.; Dupps, W.J., Jr. Comparison of Patient-Specific Computational Modeling Predictions and Clinical Outcomes of LASIK for Myopia. *Invest. Ophthalmol. Vis. Sci.* **2016**, *57*, 6287-6297, doi:10.1167/iovs.16-19948.
18. Schmitt, J. OCT elastography: imaging microscopic deformation and strain of tissue. *Opt Express* **1998**, *3*, 199-211, doi:10.1364/oe.3.000199.
19. Zvietcovich, F.; Larin, K.V. Wave-based optical coherence elastography: the 10-year perspective. *Prog Biomed Eng* **2021**, *4*, doi:10.1088/2516-1091/ac4512.
20. Ramier, A.; Eltony, A.M.; Chen, Y.; Clouser, F.; Birkenfeld, J.S.; Watts, A.; Yun, S.-H. In vivo measurement of shear modulus of the human cornea using optical coherence elastography. *Scientific Reports* **2020**, *10*, 17366, doi:10.1038/s41598-020-74383-4.
21. Hepburn, M.S.; Wijesinghe, P.; Chin, L.; Kennedy, B.F. Analysis of spatial resolution in phase-sensitive compression optical coherence elastography. *Biomed. Opt. Express* **2019**, *10*, 1496-1513, doi:10.1364/BOE.10.001496.
22. Singh, M.; Nair, A.; Aglyamov, S.R.; Larin, K.V. Compressional optical coherence elastography of the cornea. *Photonics* **2021**, *8*, 111, doi:10.3390/photonics8040111.
23. Akca, B.I.; Chang, E.W.; Kling, S.; Ramier, A.; Scarcelli, G.; Marcos, S.; Yun, S.H. Observation of sound-induced corneal vibrational modes by optical coherence tomography. *Biomed Opt Express* **2015**, *6*, 3313-3319, doi:10.1364/BOE.6.003313.
24. Li, C.; Guan, G.; Huang, Z.; Johnstone, M.; Wang, R.K. Noncontact all-optical measurement of corneal elasticity. *Opt Lett* **2012**, *37*, 1625-1627, doi:10.1364/OL.37.001625.
25. Wang, S.; Larin, K.V.; Li, J.; Vantipalli, S.; Manapuram, R.K.; Aglyamov, S.; Emelianov, S.; Twa, M.D. A focused air-pulse system for optical-coherence-tomography-based measurements of tissue elasticity. *Laser Phys Lett* **2013**, *10*, 075605, doi:10.1088/1612-2011/10/7/075605.
26. Dorronsoro, C.; Pascual, D.; Perez-Merino, P.; Kling, S.; Marcos, S. Dynamic OCT measurement of corneal deformation by an air puff in normal and cross-linked corneas. *Biomed Opt Express* **2012**, *3*, 473-487, doi:10.1364/BOE.3.000473.
27. Nair, A.; Singh, M.; Aglyamov, S.R.; Larin, K.V. Heartbeat OCE: corneal biomechanical response to simulated heartbeat pulsation measured by optical coherence elastography. *J Biomed Opt* **2020**, *25*, 1-9, doi:10.1117/1.Jbo.25.5.055001.

28. Lan, G.; Singh, M.; Larin, K.V.; Twa, M.D. Common-path phase-sensitive optical coherence tomography provides enhanced phase stability and detection sensitivity for dynamic elastography. *Biomed. Opt. Express* **2017**, *8*, 5253-5266, doi:10.1364/BOE.8.005253.
29. Jin, Z.; Chen, S.; Dai, Y.; Bao, C.; Ye, S.; Zhou, Y.; Wang, Y.; Huang, S.; Wang, Y.; Shen, M.; et al. In vivo noninvasive measurement of spatially resolved corneal elasticity in human eyes using Lamb wave optical coherence elastography. *J. Biophotonics* **2020**, *13*, e202000104, doi:10.1002/jbio.202000104.
30. Lan, G.; Aglyamov, S.R.; Larin, K.V.; Twa, M.D.J.O.; Science, V. In Vivo Human Corneal Shear-wave Optical Coherence Elastography. *Optom. Vis. Sci.* **2021**, *98*, 58-63, doi:10.1097/OPX.0000000000001633.
31. Song, S.; Huang, Z.; Nguyen, T.M.; Wong, E.Y.; Arnal, B.; O'Donnell, M.; Wang, R.K. Shear modulus imaging by direct visualization of propagating shear waves with phase-sensitive optical coherence tomography. *J Biomed Opt* **2013**, *18*, 121509, doi:10.1117/1.JBO.18.12.121509.
32. Wang, S.; Larin, K.V. Shear wave imaging optical coherence tomography (SWI-OCT) for ocular tissue biomechanics. *Opt Lett* **2014**, *39*, 41-44, doi:10.1364/ol.39.000041.
33. Ruberti, J.W.; Sinha Roy, A.; Roberts, C.J. Corneal biomechanics and biomaterials. *Annu Rev Biomed Eng* **2011**, *13*, 269-295, doi:10.1146/annurev-bioeng-070909-105243.
34. Lan, G.; Gu, B.; Larin, K.V.; Twa, M.D. Clinical corneal optical coherence elastography measurement precision: effect of heartbeat and respiration. *Transl Vis Sci Technol* **2020**, *9*, 3, doi:10.1167/tvst.9.5.3.
35. Singh, M.; Li, J.; Han, Z.; Wu, C.; Aglyamov, S.R.; Twa, M.D.; Larin, K.V. Investigating Elastic Anisotropy of the Porcine Cornea as a Function of Intraocular Pressure With Optical Coherence Elastography. *Journal of refractive surgery (Thorofare, N.J. : 1995)* **2016**, *32*, 562-567, doi:10.3928/1081597x-20160520-01.
36. Lan, G.; Aglyamov, S.; Larin, K.V.; Twa, M.D. In vivo human corneal natural frequency quantification using dynamic optical coherence elastography: repeatability and reproducibility. *J. Biomech.* **2021**, *121*, 110427, doi:10.1016/j.jbiomech.2021.110427.
37. Maczynska E; Rzeszewska-Zamiara J; Jimenez Villar A; Wojtkowski M; Kaluzny B J; I., G. Air-Puff-Induced Dynamics of Ocular Components Measured with Optical Biometry. *Invest. Ophthalmol. Vis. Sci.* **2019**, *60*, 1979-1986, doi:10.1167/iovs.19-26681.
38. Li, W.; Feng, J.; Wang, Y.; Shi, Q.; Ma, G.; Aglyamov, S.; Larin, K.V.; Lan, G.; Twa, M. Micron-scale hysteresis measurement using dynamic optical coherence elastography. *Biomed Opt Express* **2022**, *13*, 3021-3041, doi:10.1364/boe.457617.
39. Lan, G.; Shi, Q.; Wang, Y.; Ma, G.; Cai, J.; Feng, J.; Huang, Y.; Gu, B.; An, L.; Xu, J. Spatial assessment of heterogeneous tissue natural frequency using micro-force optical coherence elastography. *Frontiers in Bioengineering and Biotechnology* **2022**, 382, doi:10.3389/fbioe.2022.851094
40. Lan, G.; Xu, J.; Hu, Z.; Huang, Y.; Wei, Y.; Yuan, X.; Liu, H.; Qin, J.; Wang, Y.; Shi, Q.; et al. Design of 1300-nm spectral domain optical coherence tomography angiography system for iris microvascular imaging. *J Phys D Appl Phys* **2021**, *8*, doi:10.1088/1361-6463/abf577.
41. Hu, Z.; Rollins, A.M. Fourier domain optical coherence tomography with a linear-in-wavenumber spectrometer. *Opt Lett* **2007**, *32*, 3525-3527, doi:10.1364/ol.32.003525.
42. Lan, G.; Li, G. Design of a k-space spectrometer for ultra-broad waveband spectral domain optical coherence tomography. *Sci Rep* **2017**, *7*, 42353, doi:10.1038/srep42353.
43. Song, S.; Huang, Z.; Wang, R.K. Tracking mechanical wave propagation within tissue using phase-sensitive optical coherence tomography: motion artifact and its compensation. *J Biomed Opt* **2013**, *18*, 121505-121505, doi:10.1117/1.JBO.18.12.121505.
44. Nguyen, T.M.; Aubry, J.F.; Fink, M.; Bercoff, J.; Tanter, M. In vivo evidence of porcine cornea anisotropy using supersonic shear wave imaging. *Investigative ophthalmology & visual science* **2014**, *55*, 7545-7552, doi:10.1167/iovs.14-15127.

45. Zvietcovich, F.; Singh, M.; Ambekar, Y.S.; Aglyamov, S.R.; Twa, M.D.; Larin, K.V. Micro Air-Pulse Spatial Deformation Spreading Characterizes Degree of Anisotropy in Tissues. *IEEE journal of selected topics in quantum electronics : a publication of the IEEE Lasers and Electro-optics Society* **2021**, *27*, 6800810, doi:10.1109/jstqe.2020.3038633.
46. Sun, M.G.; Son, T.; Crutison, J.; Guaiquil, V.; Lin, S.; Nammari, L.; Klatt, D.; Yao, X.; Rosenblatt, M.I.; Royston, T.J. Optical coherence elastography for assessing the influence of intraocular pressure on elastic wave dispersion in the cornea. *Journal of the mechanical behavior of biomedical materials* **2022**, *128*, 105100, doi:10.1016/j.jmbbm.2022.105100.
47. Wang, S.; Larin, K.V. Optical coherence elastography for tissue characterization: a review. *Journal of biophotonics* **2015**, *8*, 279-302, doi:10.1002/jbio.201400108.
48. Li, J.; Han, Z.; Singh, M.; Twa, M.D.; Larin, K.V. Differentiating untreated and cross-linked porcine corneas of the same measured stiffness with optical coherence elastography. *J. Biomed. Opt.* **2014**, *19*, 110502, doi:10.1117/1.JBO.19.11.110502.